MATERIALS CHEMISTRY FRONTIERS

RESEARCH ARTICLE

View Article Online
View Journal | View Issue

Cite this: *Mater. Chem. Front.*, 2021, **5**, 3236

Stencil mask defined doctor blade printing of organic single crystal arrays for high-performance organic field-effect transistors†

Yue Xi,[a] Tao Wang,[b] Qi Mu,[b] Congcong Huang,[a] Shuming Duan,*[a] Xiaochen Ren *[a] and Wenping Hu *[a]

Received 19th January 2021,
Accepted 22nd February 2021

DOI: 10.1039/d1qm00097g

rsc.li/frontiers-materials

Organic field-effect transistors (OFETs) are one of the promising candidates for next generation electronics due to their solution processability and good performance superior to amorphous Si devices. Patterning the organic layer is necessary in practical applications to prevent cross talk between different devices. Here, we reported a novel solution processed, high-resolution patterning method named as stencil mask defined doctor blade printing to fabricate regularly patterned organic single crystal arrays. The size of one pattern is around 30 μm, which is smaller than the droplet diameter of conventional inkjet printing. The OFETs based on organic single crystal patterns exhibit extremely low off-state current and high on/off current ratio close to 10^{10} as well as good device uniformity. The low off-state current demonstrates the potential of the OFET array for low-power or high-performance optical sensing applications. In addition, the short channel OFET array exhibits good frequency response operating at 20 kHz. This work provides an effective patterning strategy to realize solution processed large-area, high-resolution organic single crystal arrays.

1. Introduction

Organic field-effect transistors (OFETs) are the basic building blocks to construct organic integrated circuits.[1–3] They are promising candidates for next-generation electronic applications[4,5] because of their mechanical flexibility,[6] high-performance comparable to oxide semiconductors,[7] and solution processability.[8] The solubility of organic semiconductors (OSCs), including small molecular weight materials and conjugated polymers, enable cost-effective manufacturing of OSCs by various printing methods to realize high-throughput and continuous fabrication.[9,10] To optimize device performance, organic single crystal semiconductors are preferred because of their grain boundary free nature to miniaturize the defect density,[11] ensuring excellent and uniform electronic characteristics.[12,13] Moreover, to reach a higher level of integration, OFETs are always in an array form with high spatial resolution.[14] These applications require the precise patterning of OSC thin films.[15,16] Well-patterned OSCs can avoid unwanted leakage current, lower the off-state current and reduce crosstalk between neighboring devices.[17,18] Single crystal OSC arrays would be ideal for high-performance organic integrated circuits with excellent uniformity and reproducibility.[19–22] However, challenges remain to fabricate organic single crystal arrays with high-resolution by printing methods.[23–25]

Unlike inorganic semiconductors, conventional photolithography processes may not be applicable for OSCs, because the organic semiconductor would be damaged by processing chemicals or high temperature.[17,26] Inkjet printing is a promising technology to fabricate large-scale organic electronic device arrays due to its drop-on-demand characteristic and moderate resolution.[27–29] Organic patterns are formed by jetting the droplets, so the minimum resolution of one pattern is equal to the diameter of the droplet, typically ranging from 30 to 100 μm.[10,30] Further reducing the droplet size may require complex technologies such as electrohydrodynamic jet (E-jet) printing.[31] Moreover, the uncontrolled nucleation of organic materials during solidification of droplets results in polycrystalline or amorphous organic thin films.[9,32,33] Other than printing, several approaches have been applied to pattern organic semiconductors.[34,35] Wang and co-workers employed photolithography-patterned Au electrodes to alter the surface properties of the substrate, and thus to selectively grow TES-ADT single crystals in an array form.[36] Self-assembled monolayers and pre-patterned stamps were also employed to direct the

[a] *Tianjin Key Laboratory of Molecular Optoelectronic Sciences, Department of Chemistry, School of Science, Tianjin University & Collaborative Innovation Center of Chemical Science and Engineering (Tianjin), Tianjin, 300072, China. E-mail: duanshm@tju.edu.cn, renxiaochen@tju.edu.cn, huwp@tju.edu.cn*

[b] *School of Microelectronics, Tianjin University, Tianjin, 300072, China*

† Electronic supplementary information (ESI) available. See DOI: 10.1039/d1qm00097g

nucleation of molecules and subsequent growth of organic crystals. Park *et al.* prepared highly aligned and patterned transistor arrays with a high density by a differential surface energy and solution shearing method.[37] Hasegawa and co-workers obtained a large single crystal array of organic semiconductor C_8-BTBT by combining inkjet printing with the solvent–antisolvent crystallization approach.[38] However, unlike the low-cost printing process, these methods still require direct photolithography to define the wetting/dewetting region for patterning the organic solution.[17,34,35] In addition, multiple grain boundaries are presented in organic thin films, which may increase the device-to-device variation.[39–41]

In this work, we demonstrated a method to realize solution processed organic single crystal arrays with spatial resolution down to 30 μm, which is smaller than the average droplet size of conventional inkjet printing. A large-area continuous organic single crystalline thin film is first fabricated by using solution shearing, and then covered by a patterned aqueous resist deposited by stencil mask defined doctor blade printing. The aqueous resist defines the pattern of organic single crystals and was finally removed by water rinsing. The patterned single crystal OSC array effectively reduced the parasitic current of the OFET device, resulting in an on/off current ratio close to 10^{10} on a SiO_2 dielectric and 10^8 within 3 V gate bias on an AlO_x dielectric, respectively. The OFET array based on highly oriented OSCs shows good device uniformity. This method demonstrates the potential of printed organic transistors for high-performance, high-resolution organic integrated circuit applications.

2. Results and discussion

Stencil mask defined doctor blade printing

Previously, we demonstrated a new strategy to fabricate organic single crystal array all by solution methods.[42] The solution shearing of C_8-BTBT/PS blend ink provides a centimeter-scale continuous highly crystalline organic thin film. Because the solution shearing method provides a strong directional convective flow in organic ink, by which the fastest crystal growth axis of the material is easy to align with the coating direction. The insulating polymer in the blended ink also helps to improve the crystallinity of the organic thin film. Then the PVA resist is screen printed on top of the organic layer to form the patterns by performing wet or dry etching. The resulting organic patterns are highly crystalline and share very similar crystal orientation and quality because they originated from the same crystalline thin film. The patterning resolution of the organic layer is determined by the screen mask used for screen printing. In particular, the open mesh aperture of the emulsion coated on the screen mesh defines the printing resolution of screen printing, which is formed by a lithography method.[43] The minimum size of opening of the emulsion should be larger than the square root of two times the wire diameter of the screen mesh, as shown in Fig. 1a, otherwise the screen mesh would completely block the open mesh aperture of the emulsion. Therefore, the screen-printing resolution is limited by the wire diameter of the screen mesh. A routinely achievable resolution of screen printed PVA resists ranges from 80 to 100 μm.

To overcome the limitations of the screen mesh, we apply a new printing method by replacing the screen mask with a meshless stencil mask made by a molybdenum thin film, named as stencil mask defined doctor blade printing to enhance the printing resolution. The deposition of the PVA resist is realized by pressing the PVA solution through a patterned molybdenum stencil with a doctor blade as shown in Fig. 1b. Homemade printing equipment is built to maintain a small distance between the stencil mask and substrate. A doctor blade is moved across the mask to progressively fill the open mesh apertures with PVA resist, and the elastic deformation of the stencil mask produces a reverse stroke to cause the mask to

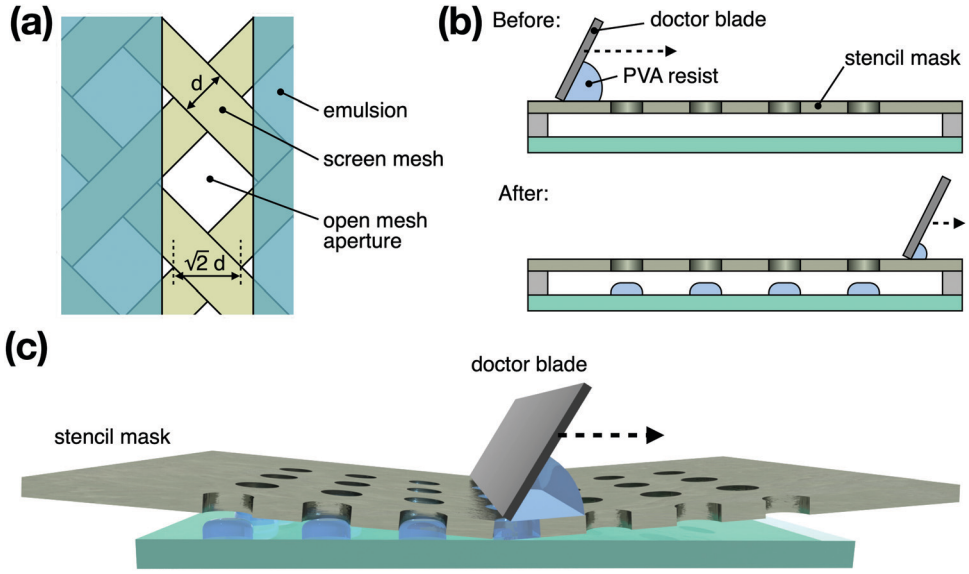

Fig. 1 (a) The schematic drawing of the screen mesh and emulsion of the screen mask. (b) The schematic drawing of the stencil mask defined doctor blade printing process, where the PVA resist is filled and patterned by the stencil mask. (c) Cross-sectional illustration of the stencil during printing.

touch the substrate momentarily along the line of contact, as depicted in Fig. 1c. The meshless nature of the molybdenum stencil enables high-resolution printing of the resist. In this work, the molybdenum stencil is pre-patterned by acid corrosion with a resolution of 30 μm.

To fabricate a high-resolution organic crystalline array, a large-area highly crystalline C_8-BTBT/PS blend thin film is prepared by solution shearing at first (Fig. S1, ESI†). The surface of the C_8-BTBT single crystal is hydrophobic with a water contact angle of 102.8°, as shown in Fig. 2a. Although PVA can act as a surfactant in aqueous solution to improve surface wetting, especially at higher concentrations,[42] the contact angle of the PVA droplet on the C_8-BTBT crystal remains close to 90° (Fig. 2a). In this work, we intentionally use the surface tension of PVA droplets to form a round shaped resist pattern. As a result, the printed 36 wt% PVA aqueous resist has a round shape by using a circular opening stencil mask with a diameter of 30 μm. The overall 1 cm^2 printed area and its zoomed-in picture are shown in Fig. 2b and c, respectively. As depicted in Fig. 2b, over 1764 patterns are evenly distributed on 1 cm^2 C_8-BTBT crystalline thin film. The enlarged Fig. 2c suggests that the average diameter of PVA resist patterns is around 30–40 μm. The statistics of the diameter of the patterns shown in Fig. 2b and c are obtained by applying image processing and plotted in Fig. S2 (ESI†). In Fig. 2b, nearly 85% of the PVA patterns have a diameter ranging from 25 to 35 μm, while the patterns close to the edge slightly deviate from the average size. This is probably due to the higher tension at the edge of the stencil mask during printing and could be improved by increasing the stencil size. The detailed 3D geometry information of the printed PVA resist patterns is measured by Leica DCM8 optical surface measurement equipment and shown in Fig. 2d. The thickness of the resist is around 2 μm with sharp edges, demonstrating the potential for further reducing the pattern size. All the results in Fig. 2b–d indicate high patterning density, high-resolution and good printing quality of stencil mask defined doctor blade printing.

High-resolution OSC single crystal array

The completion of the OSC single crystal array is fabricated by plasma etching for 40 s followed by water rinsing. To investigate the crystallinity of the as-fabricated C_8-BTBT single crystal array, we performed various characterization techniques including polarized optical microscopy (POM), atomic force microscopy (AFM), selected area electron diffraction (SAED), and X-ray diffraction (XRD). The POM images of the OSC array in Fig. 3a and b show that every element in the array has a uniform shape and diameter around 30 μm. When rotating the sample by 45°, all the elements in the array show simultaneous color changing, indicating that they all have the same crystal orientation as well as very similar film thickness and crystal quality. This characteristic is essential for minimizing device-to-device variation of OFETs. Fig. 3c and d show the enlarged POM images of the single crystal array. Within each pattern, there is no grain boundary presented, the color difference in the POM images is due to the thickness variation of the organic crystal. The typical dendritic growth surface morphology is observed for the C_8-BTBT material.[44] Notice that the 30 μm diameter of the patterns is smaller than one droplet size of conventional inkjet printed OSCs. Moreover, compared to inkjet printing, our method produces a highly aligned, grain boundary free organic crystal array and better patterning uniformity.

The atomic force microscopy (AFM) picture in Fig. 4a shows that the smallest diameter of the pattern is smaller than 25 μm. The average root-mean-square roughness of the pattern is

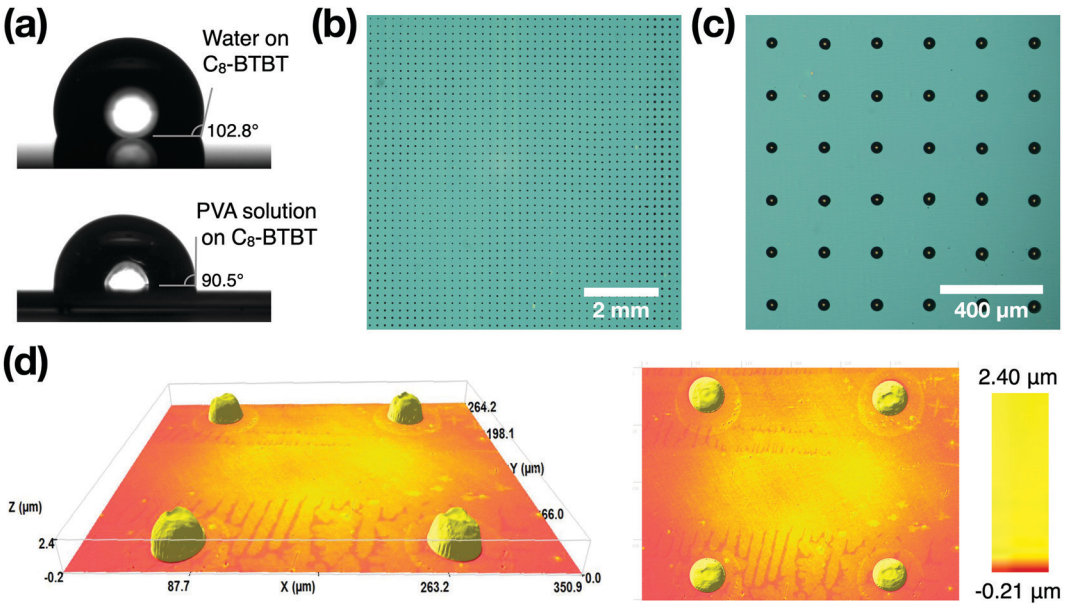

Fig. 2 (a) The contact angle of water and the PVA resist solution on the C_8-BTBT crystalline thin film. The contact angle of water and PVA is 102.8° (above) and 90.5° (below), respectively. (b) An optical image of the printed PVA array on C_8-BTBT with an area of 1 cm^2. (c) The zoomed-in image of the printed PVA array on C_8-BTBT. (d) 3D geometry information of printed PVA resist patterns.

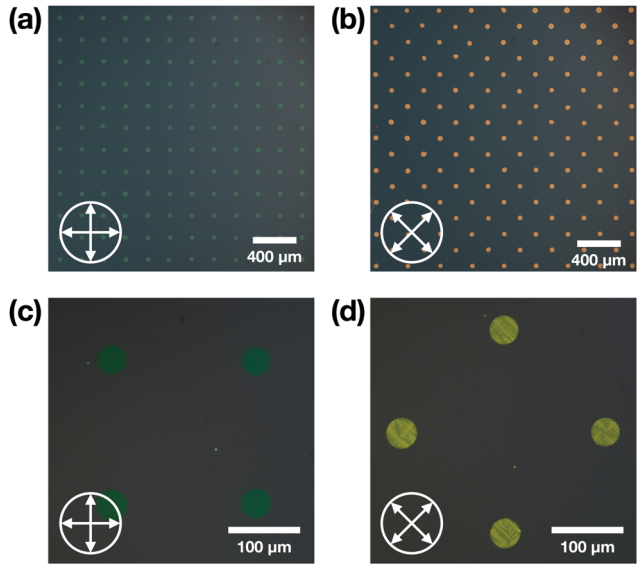

Fig. 3 (a and b) The polarized optical microscopy (POM) images of the patterned C_8-BTBT single crystal array on the SiO_2 surface. (c and d) The zoomed-in POM images of the patterned C_8-BTBT single crystal array on the SiO_2 surface.

0.68 nm, suggesting that the C_8-BTBT has a smooth surface close to the atomic level. As shown in Fig. 4b, the thickness of one C_8-BTBT single crystal pattern is 18.6 nm. For a 20 mg mL^{-1} of 1 : 1 C_8-BTBT/PS blending ratio, the thickness of C_8-BTBT is around 8.8 nm, corresponding to three molecular layers.[45] The thin thickness and good surface quality are beneficial for reducing the organic bulk resistance at the source/drain contact, resulting in improved charge injection in OFETs. For SAED measurement, as shown in Fig. 4c, the sharp diffraction spots in the SAED pattern indicate a highly crystallized structure of the organic thin film. Lattice constants calculated from the SAED pattern (a = 5.8 Å, b = 7.8 Å, γ = 90.7) agree well with reported C_8-BTBT bulk crystal data.

The crystalline properties and crystal packing are further studied by examining X-ray diffraction (XRD) of the C_8-BTBT single crystal array as shown in Fig. 4d. The out-of-plane XRD profile presents a smooth baseline and sharp diffraction peaks indicating the highly ordered and crystalline quality of C_8-BTBT. The corresponding secondary diffraction peaks were also observed, manifesting the layer-by-layer growth of organic semiconductor molecules on the substrate. Moreover, these diffraction peaks correspond well to the crystal structure of C_8-BTBT reported previously,[46] which indicates that the ab-plane is parallel to the substrate. We performed in-plane XRD for organic crystalline thin films before patterning. The results depicted in Fig. 4e and f show one strong Bragg diffraction peak (020) when the incident X-ray beam is parallel to the shearing direction ($\phi = 0^\circ$), while the (020) peak decays quickly, and strong (110) and (120) peaks were observed when the sample rotates around the ϕ axis by 90°, indicating that all the patterns in the array are highly crystalline in the in-plane direction and the a-axis of all the C_8-BTBT patterns are roughly parallel to the shearing direction.[47] The presence of the (120) peak in Fig. 4d suggests that there are a small portion of molecules in the array oriented in a different direction.[48]

Electrical characteristics of the single crystal OFET array

To characterize the electrical properties of the patterned OSC arrays, bottom-gate and top-contact organic field-effect transistors (OFETs) were fabricated on a SiO_2/Si substrate finished by thermally evaporated Ag (40 nm) used as source/drain electrodes combined with a 5 nm F_4-TCNQ injection layer. As shown by the optical image depicted in Fig. 5a, the fine copper grid was used as a shadow mask, and the channel width and length of the OFET are 20 and 5 μm, respectively. Fig. 5b shows a representative transfer I–V characteristic of a patterned C_8-BTBT OFET. The unit-area capacitance (C_i) of the dielectric, which consists of phase separation formed PS and SiO_2 is measured to be 10.6 nF cm^{-2} (Fig. S3, ESI†). In Fig. 5b, the transistor exhibits a standard p-type FET I–V characteristic behavior with a high on/off current ratio close to 10^{10}, which can be attributed to the patterning induced low off-state current. Patterning the OSC eliminates most of the unwanted fringe current from the lateral path, leading to extremely low off-state current. The carrier mobility estimated from the slope of the transfer I–V curve is 2.34 $cm^2\ V^{-1}\ s^{-1}$, which is lower than the reported value of the same OSC on a SiO_2 dielectric.[42] The reason for the decreased mobility is probably due to the short channel length of the OFET so that the contact resistance becomes more significant compared to the channel resistance. Therefore, the drain–source voltage (V_{DS}) applied on the channel has been reduced because of the voltage drop on contact resistance, and thus the apparent mobility of the device is decreased. The nonlinearity of the output I–V at a small V_{DS} region proves the existence of contact resistance (Fig. 5c). Because all of the patterns are inherited from the same organic crystalline thin film, the device array exhibits uniform electrical characteristics. As depicted in Fig. 5d and in Fig. S4 (ESI†), the standard deviation of mobility and threshold voltage (V_{th}) is 0.59 $cm^2\ V^{-1}\ s^{-1}$ and 1.48 V, respectively.

Low voltage single crystal OFET array

To demonstrate the low-power applications of the high-resolution patterning method, we fabricated a low-voltage OFET array on an anodized AlO_x dielectric layer. The representative transfer I–V curve for a patterned C_8-BTBT single crystal OFET is shown in Fig. 6a. The saturation mobility and the threshold voltage of the device is 1.53 $cm^2\ V^{-1}\ s^{-1}$ and −0.74 V, respectively. The C_i of PS/AlO_x is measured to be 174 nF cm^{-2} shown in Fig. S5 (ESI†). Except from a battery range operating voltage benefited from high-k dielectric, the on/off current ratio of the OFET is as large as 10^8 within −3 V gate bias. The patterned OSC layer effectively reduces the fringe current as well as possible gate leakage current, resulting in a relatively low off-state current in the range of several tens of fA. Therefore, the on/off current ratio of the low-voltage OFET reaches over 10^8. To confirm this result, we measured eight devices and the averaged on/off ratio is larger than 10^8 (Fig. S6, ESI†). We summarize the device parameters of recently reported low voltage OFETs as listed in Table 1. It is clear that

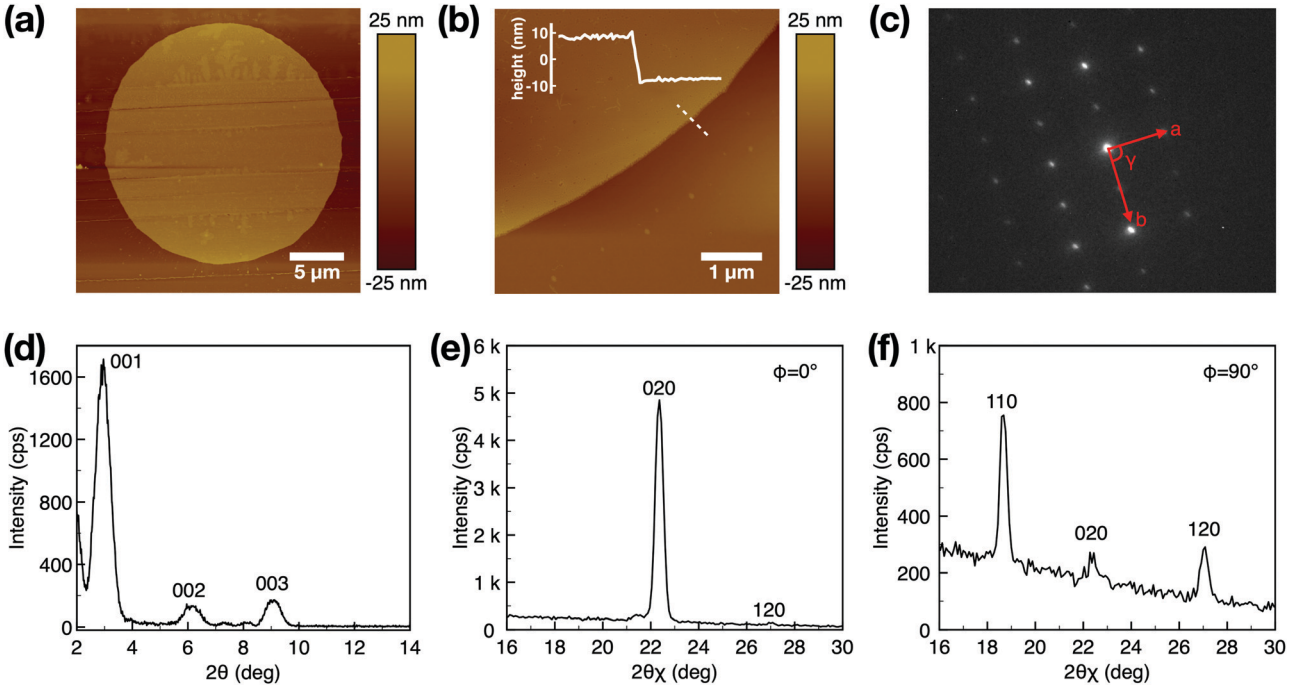

Fig. 4 (a) Atomic force microscopy (AFM) image of a single C_8-BTBT pattern. (b) Detailed AFM image of one pattern; the white line indicates the cross-section profile of the pattern, and the thickness of the pattern is around 18.6 nm. (c) Selected area electron diffraction (SAED) patterns of a C_8-BTBT single crystal. (d) Out-of-plane X-ray diffraction (XRD) profile of the C_8-BTBT single crystal array. (e and f) In-plane XRD profile of the C_8-BTBT crystalline thin film where the shearing direction is parallel and perpendicular to the incident X-ray beam, respectively.

nearly two orders of magnitude enhancement of the on/off current ratio have been achieved, which is attributed to the patterned OSCs. The extremely low off-state current also largely reduces the static power consumption of OFETs, proving its suitability for low-power applications. Furthermore, the off-state current is directly related to the noise equivalent power of a phototransistor device, and reducing the off-state current could significantly enhance the specific detectivity and dynamic range of the phototransistor, demonstrating the potential of this device for high-performance optical sensing applications.

Dynamic response characteristics of OFETs

The OFETs based on high-resolution OSC patterns benefit high frequency operation. Here, a simple circuit is applied to evaluate the frequency response of the OFET as shown in Fig. 6b. Although high carrier mobility is required for high-speed device applications, the device dimension also plays a critical role in improving the operation frequency,[13] because the cut-off frequency of an OFET is determined predominantly by the total resistance and parasitic capacitance of a transistor as shown in eqn (1).

$$f_T = \frac{\mu_{eff} V_D}{2\pi L(L + L_C)} \quad (1)$$

where μ_{eff} is the effective mobility, V_D is the drain–source voltage, L and L_C are channel length and the total overlap length between the gate and the source/drain electrodes, respectively. In the current device, the channel length is 5 μm and $L + L_C$ is equal to the diameter of the pattern, which is 30 μm. To characterize the dynamic response of the OFET, we serially connect a resistor to the OFET as a constant load inverter and applied an AC input voltage to the gate. As shown in Fig. 6c, the output voltage that was applied on the resistor periodically changes at 8 V 500 Hz square wave V_{in} signal. The output voltage of the OFET at different frequencies is plotted in Fig. S7 (ESI†). A distinguishable output oscillation signal is observed at frequency up to 20 kHz.

The characteristic rise time t_{rise} refers to the time for the output signal to rise from '0' to '1' while the fall time t_{fall} refers to the time for the output signal to fall from '1' to '0'. In particular, t_{rise} is the time to rise from 10% value of '0' to 90% value of the '1' state. And t_{fall} is the time to fall from 90% value of '1' to 10% value of the '0' state. By fitting the simple exponential functions to the measured output voltage data, the t_{rise} and t_{fall} are determined to be 303 μs and 618 μs, respectively. The t_{rise} and t_{fall} can also be calculated based on time constant τ_p and τ_n, following the formula $t_{rise} = 2.2\tau_p$ and $t_{fall} = 2.2\tau_n$, in which τ_p and τ_n are the time constants of the exponential function obtained from data fitting. The maximum signal frequency of the system is defined by $f_{max} = 1/(t_{rise} + t_{fall})$, which is estimated to be 1.08 kHz in this work. Besides, the propagation delay t_p of the system, which reflects how fast the device output reacts to input change, can be calculated by $t_p = 0.5(t_{prise} + t_{pfall})$, where the rise propagation delay t_{prise} and fall propagation delay t_{pfall} are the time for the output signal to increase or fall by 50%, respectively. Ideally, if the input voltage is step changed, it would satisfy the relationship of $t_{prise} = \ln(2)\tau_p$ and $t_{pfall} = \ln(2)\tau_n$. The total propagation delay is

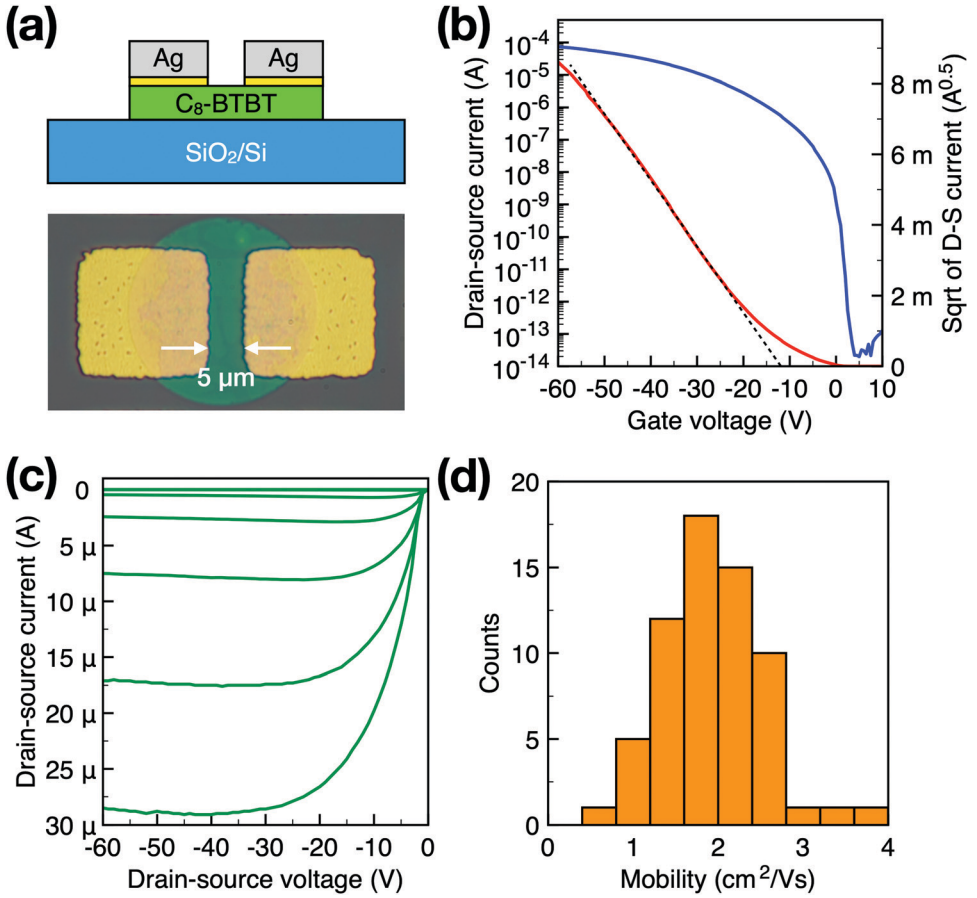

Fig. 5 (a) The schematic drawing of a patterned C_8-BTBT OFET on a SiO_2/Si substrate; the orange lines represent a 5 nm thick F_4-TCNQ charge injection layer between the top electrodes and organic semiconductor, and the channel width and length of the OFET are 20 μm and 5 μm, respectively. (b) The transfer I–V curve and (c) the output I–V curve of a patterned C_8-BTBT OFET on a SiO_2/Si substrate. (d) The saturation mobility histogram of 64 randomly selected devices; the average value is 1.91 $cm^2\ V^{-1}\ s^{-1}$ and the standard deviation is 0.59 $cm^2\ V^{-1}\ s^{-1}$.

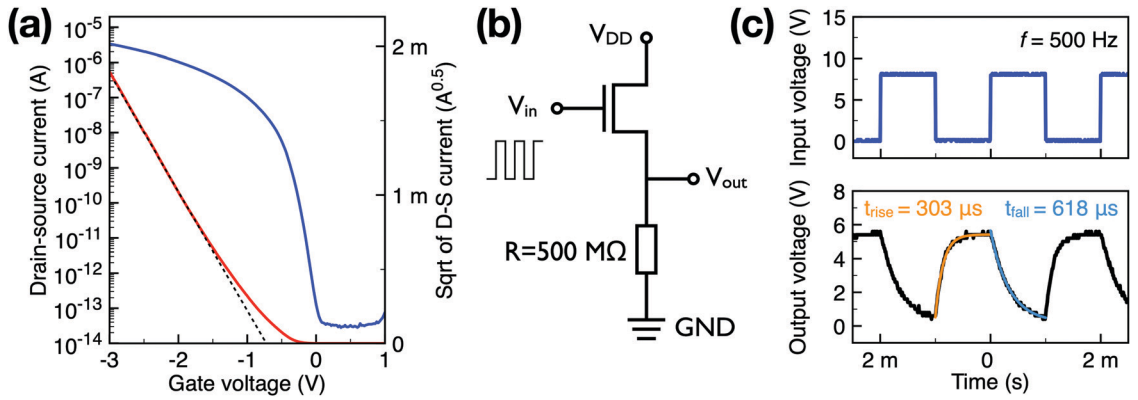

Fig. 6 (a) A representative transfer I–V curve of a patterned C_8-BTBT OFET on an AlO_x/Al substrate. (b) Circuit diagram of a resistor load inverter based on a patterned C_8-BTBT OFET. (c) Dynamic characteristics of the inverter in response to an AC input voltage signal with a frequency of 500 Hz, a duty cycle of 50%, and an amplitude of 8 V. Characteristic rise and fall time constants of the switching delays (t_{rise}, t_{fall}) were determined by fitting simple exponential functions to the measured output waveform.

measured by $t_p = 0.35(\tau_n + \tau_p)$, which is 166.99 μs in this work. The above-mentioned characteristic time of the device is summarized in Table 2, where the value obtained from theoretical calculation is marked with a star. Benefited from the high-resolution OSC pattern and short channel length, the OFET can operate above kHz range, while further optimization is necessary by reducing the contact resistance for short channel devices.

Table 1 The device parameters of recently reported low voltage OFETs

Semiconductor material	Crystallinity	OFET structure	Saturation V_G (V)	On/off ratio	SS (mV dec^{-1})	Mobility (cm^2 V^{-1} s^{-1})	Channel length (μm)	W/L	Ref.
C_8-DNBDT-NW	Single-crystal	BGTC	−1.5	10^6	98	6.60	100	1	49
diF-TES-ADT	Crystalline	BGBC	−10	$>10^4$	—	0.20	50	10	50
DPPT-TT	Amorphous	TGBC	−10	$>10^6$	439	0.11	65	15	51
TIPS-pentacene	Amorphous	BGBT	−3	10^4	130	0.25	100	200	52
TIPS-pentacene	Crystalline	BGTC	−5	10^5	550	7.00	150	8	53
C_9-DNBDT-NW	Single crystal	BGTC	−4	$>10^{10}$	—	8.60	5	200	54
PIDT-BT	Amorphous	TGBC	−3	10^5	—	4.65	150	150	55
TIPS-pentacene	Amorphous	BGBC	−4	10^3	500	0.20	200	100	56
DPP-DTT	Amorphous	BGTC	−10	10^5	590	0.30	50	20	57
C_{10}-DNTT	Amorphous	BGBC	−3	10^5	110	1.8	30	3	58
C_8-BTBT	Amorphous	BGTC	−5	$>10^6$	87.4	3.39	200	5	59
TIPS-pentacene	Crystalline	BGTC	−5	10^5	460	0.43	150	10	60
C_8-BTBT	Single-crystal	BGTC	−3	10^8	107	1.53	5	4	This work

Table 2 Transient parameters of dynamic response of the resistor load inverter

Rise time and fall time		Theoretical value	Maximum signal frequency
τ_p: 138.1 μs	t_{rise}: 303 μs	t^*_{rise}: 303.82 μs	f_{max}: 1.08 kHz
τ_n: 339 μs	t_{fall}: 618 μs	t^*_{fall}: 745.8 μs	
Propagation delay		**Theoretical value**	
t_{pfall}: 240 μs		t^*_{pfall}: 234.98 μs	
t_{prise}: 100 μs		t^*_{prise}: 95.72 μs	
t_p: 170 μs		t^*_p: 166.99 μs	

$t^*_{rise} = 2.2\tau_p$, $t^*_{fall} = 2.2\tau_n$, $t^*_{prise} = \ln(2)\tau_p$, $t^*_{pfall} = \ln(2)\tau_n$, $t^*_p = 0.35(\tau_p + \tau_n)$.

3. Conclusions

In summary, we have demonstrated a novel stencil mask defined doctor blade printing method to realize high-resolution OSC single crystal arrays. The application of a stencil mask provides a pattern resolution smaller than one droplet of inkjet printing. All the elements in the array have the same crystal orientation as well as very similar film thickness and crystal quality. The patterned OSC eliminates most of the unwanted fringe current from the lateral path as well as the possible contribution from gate leakage current in OFETs, leading to extremely low off-state current and high on/off current ratio close to 10^{10} on the SiO_2 dielectric and 10^8 within 3 V gate bias on the AlO_x dielectric, respectively. The low off-state current demonstrates the potential of the device array for low-power or high-performance optical sensing applications. Moreover, the short channel OFET array exhibits good frequency response operating at 20 kHz. Our results provide an effective patterning strategy to realize solution processed large-area, high-resolution organic single crystal arrays.

4. Experimental

Materials

Chlorobenzene (anhydrous, 99.8%), PS (analytical standard, average molecular weight: ≈2 000 000), and C_8-BTBT (≥99%) were bought from Sigma-Aldrich. PVA-203 (molecular weight: ≈31 000) was purchased from Aladdin. The heavily n-doped Si wafer with thermally grown 300 nm SiO_2 was bought from China Electronics Technology Group Corporation. The glass slide was purchased from Biologix Group. All materials were used directly without further purification. The molybdenum stencil was custom made from Beijing Xinxing Bairui Limited, China.

Stencil mask defined doctor blade printing

An aqueous solution of PVA (36 wt%) was utilized for printing. The 20 μm thick molybdenum stencil mask with a 30 μm diameter circular array opening is placed 1 mm above the substrate. A plastic blade is used to perform printing.

Device fabrication

Top contact bottom gate OFETs were fabricated on the SiO_2/Si and glass substrate, respectively. The substrates were cleaned by sonicating in deionized water, acetone and isopropanol for 5 mins separately, and then dried by nitrogen flow. For OFETs on a high-k AlO_x dielectric, 100 nm Al was thermally evaporated at 40 Å s^{-1}, the sample was then put into sodium citrate/citrate acid solution for anodization. The details of anodization can be found in our previous studies.[61] The C_8-BTBT and PS in a 1 : 1 blend ratio were dissolved into chlorobenzene with a concentration of 20 mg mL^{-1}. The blended solution was coated on the different substrates by homemade solution-shearing equipment for single crystal growth. The shearing speed was about 0.3 mm s^{-1}, and the substrate is heated to 40 °C. After the printing of the PVA array, the sample was dry etched by oxygen plasma for 40 s, at the power of 20 W. Then the PVA was rinsed by water dipping. The sample was then annealed at 60 °C for 30 mins to remove residual solvent. Finally, 40 nm Ag top electrodes and a 5 nm F_4-TCNQ injection layer underneath were deposited by thermal evaporation. A fine 1000 square-hole copper mesh (Xinxing Bairui Limited) for placing the transmission electron microscope (TEM) samples was used as the shadow mask during thermal evaporation. The rib width of the copper mesh is 5 μm. The channel width and length of the OFET is 20 μm and 5 μm, respectively.

Characterization

OM and POM images were captured by a Nikon Eclipse Ci-POL polarized microscope. 3D morphology pictures were captured by a Leica DCM8 optical surface measurement system. AFM images were obtained with Intelligent-mode using a Bruker Dimension Icon in air. In-plane and out-of-plane XRD data were obtained by a Rigaku SmartLab X-ray diffractometer with the highest power of 9 kW. The transfer and output *I–V* curves of the OFETs were measured by a Keithley 4200 SCS semiconductor parameter analyzer equipped with a remote preamplifier. The field-effect mobility of the OFET at the saturation region was measured by $I_{DS} = \mu C_i W(V_G - V_{th})^2/2L$. For frequency response measurement, RIGOL DG822 is used to generate the input voltage. The V_{in} and V_{out} voltage signals were recorded by a Tektronix TDS 1002C oscilloscope.

Author contributions

Yue Xi: conceptualization, formal analysis, investigation, methodology, writing – original draft. Tao Wang: methodology, investigation. Qi Mu: investigation, validation. Congcong Huang: investigation. Shuming Duan: methodology, supervision. Xiaochen Ren: methodology, data curation, project administration, writing – review & editing. Wenping Hu: funding acquisition, project administration, resources.

Conflicts of interest

There are no conflicts to declare.

Acknowledgements

This work was financially supported by the Ministry of Science and Technology of China (Grants 2018YFA0703200), the National Natural Science Foundation of China (91833306, 51633006, 51703160, 51733004, 51725304, and 52003189), and the China Postdoctoral Science Foundation (2020M680875).

Notes and references

1 H. Chen, W. Zhang, M. Li, G. He and X. Guo, Interface Engineering in Organic Field-Effect Transistors: Principles, Applications, and Perspectives, *Chem. Rev.*, 2020, **120**, 2879–2949.
2 T. Leydecker, Z. M. Wang, F. Torricelli and E. Orgiu, Organic-based inverters: basic concepts, materials, novel architectures and applications, *Chem. Soc. Rev.*, 2020, **49**, 7627–7670.
3 K. S. Park, J. Baek, Y. Park, L. Lee, J. Hyon, Y. E. Koo Lee, N. K. Shrestha, Y. Kang and M. M. Sung, Heterogeneous Monolithic Integration of Single-Crystal Organic Materials, *Adv. Mater.*, 2017, **29**, 1603285.
4 S. Yuvaraja, A. Nawaz, Q. Liu, D. Dubal, S. G. Surya, K. N. Salama and P. Sonar, Organic field-effect transistor-based flexible sensors, *Chem. Soc. Rev.*, 2020, **49**, 3423–3460.
5 S. Wang, J. Xu, W. Wang, G. Wang, R. Rastak, F. Molina-Lopez, J. Chung, S. Niu, V. Feig, J. Lopez, T. Lei, S. Kwon, Y. Kim, A. Foudeh, A. Ehrlich, A. Gasperini, Y. Yun, B. Murmann, J. B.-H. Tok and Z. Bao, Skin electronics from scalable fabrication of an intrinsically stretchable transistor array, *Nature*, 2018, **555**, 83–88.
6 Y. Wang, L. Sun, C. Wang, F. Yang, X. Ren, X. Zhang, H. Dong and W. Hu, Organic crystalline materials in flexible electronics, *Chem. Soc. Rev.*, 2019, **48**, 1492.
7 H. Sirringhaus, 25th anniversary article: organic field-effect transistors: the path beyond amorphous silicon, *Adv. Mater.*, 2014, **26**, 1319–1335.
8 S. G. Higgins, B. V. Muir, J. Wade, J. Chen, B. Striedinger, H. Gold, B. Stadlober, M. Caironi, J. Kim, J. H. G. Steinke and A. J. Campbell, Self-aligned megahertz organic transistors solution-processed on plastic, *Adv. Electron. Mater.*, 2015, **1**, 1500024.
9 L. Kong, C. Tang, H. J. Peng, J. Q. Huang and Q. Zhang, Advanced energy materials for flexible batteries in energy storage: A review, *SmartMat*, 2020, **1**, e1007.
10 K. Fukuda and T. Someya, Recent progress in the development of printed thin-film transistors and circuits with high-resolution printing technology, *Adv. Mater.*, 2016, **29**, 1602736.
11 X. Zhang, H. Dong and W. Hu, Organic semiconductor single crystals for electronics and photonics, *Adv. Mater.*, 2018, **30**, 1801048.
12 Y. Yao, Y. Chen, H. Wang and P. Samorì, Organic photodetectors based on supramolecular nanostructures, *SmartMat*, 2020, **1**, e1009.
13 A. Yamamura, T. Sakon, K. Takahira, T. Wakimoto, M. Sasaki, T. Okamoto, T. Okamoto and J. Takeya, High-Speed Organic Single-Crystal Transistor Responding to Very High Frequency Band, *Adv. Funct. Mater.*, 2020, **30**, 1909501.
14 P. K. L. Chan, The Motivation for and Challenges to Scaling Down Organic Field-Effect Transistors, *Adv. Electron. Mater.*, 2019, **5**, 1900029.
15 Y. Liu, J. Feng, B. Zhang, Y. Wu, Y. Chen and L. Jiang, Regular Aligned 1D Single-Crystalline Supramolecular Arrays for Photodetectors, *Small*, 2018, **14**, 1701861.
16 W. Deng, Y. Lv, X. Zhang, X. Fang, B. Lu, Z. Lu and J. Jie, High-resolution patterning of organic semiconductor single crystal arrays for high-integration organic field-effect transistors, *Mater. Today*, 2020, **40**, 82.
17 X. Zhang, W. Deng, R. Jia, X. Zhang and J. Jie, Precise Patterning of Organic Semiconductor Crystals for Integrated Device Applications, *Small*, 2019, **15**, 1900332.
18 K. Pei, M. Chen, Z. Zhou, H. Li and P. K. L. Chan, Overestimation of carrier mobility in organic thin film transistors due to unaccounted fringe currents, *ACS Appl. Electron. Mater.*, 2019, **1**, 379–388.
19 S. Kumagai, A. Yamamura, T. Makita, J. Tsurumi, Y. Y. Lim, T. Wakimoto, N. Isahaya, H. Nozawa, K. Sato, M. Mitani, T. Okamoto, S. Watanabe and J. Takeya, Scalable fabrication of organic single-crystalline wafers for reproducible TFT arrays, *Sci. Rep.*, 2019, **9**, 1–8.

20 K. Kim, K. Nam, X. Li, D. Y. Lee and S. H. Kim, Programmed Design of Highly Crystalline Organic Semiconductor Patterns with Uniaxial Alignment via Blade Coating for High-Performance Organic Field-Effect Transistors, *ACS Appl. Mater. Interfaces*, 2019, **11**, 42403–42411.
21 X. Zhao, X. Ding, Q. Tang, Y. Tong and Y. Liu, Photolithography-compatible conformal electrodes for high-performance bottom-contact organic single-crystal transistors, *J. Mater. Chem. C*, 2017, **5**, 12699–12706.
22 X. Zhang, J. Mao, W. Deng, X. Xu, L. Huang, X. Zhang, S.-T. Lee and J. Jie, Precise Patterning of Laterally Stacked Organic Microbelt Heterojunction Arrays by Surface-Energy-Controlled Stepwise Crystallization for Ambipolar Organic Field-Effect Transistors, *Adv. Mater.*, 2018, **30**, 1800187.
23 K. S. Park, J. Baek, Y. Park, L. Lee, Y. E. K. Lee, Y. Kang and M. M. Sung, Inkjet-Assisted Nanotransfer Printing for Large-Scale Integrated Nanopatterns of Various Single-Crystal Organic Materials, *Adv. Mater.*, 2016, **28**, 2874–2880.
24 K. Kim, J. Bae, S. H. Noh, J. Jang, S. H. Kim and C. E. Park, Direct Writing and Aligning of Small-Molecule Organic Semiconductor Crystals via ''Dragging Mode'' Electrohydrodynamic Jet Printing for Flexible Organic Field-Effect Transistor Arrays, *J. Phys. Chem. Lett.*, 2017, **8**, 5492–5500.
25 Y. Zhao, X. Fan, J. Feng, X. Wang, Y. Wu, B. Su and L. Jiang, Regulated Dewetting for Patterning Organic Single Crystals with Pure Crystallographic Orientation toward High Performance Field-Effect Transistors, *Adv. Funct. Mater.*, 2018, **28**, 1800470.
26 Y. Yao, L. Zhang, T. Leydecker and P. Samorì, Direct Photolithography on Molecular Crystals for High Performance Organic Optoelectronic Devices, *J. Am. Chem. Soc.*, 2018, **140**, 6984.
27 S. Chung, K. Cho and T. Lee, Recent progress in inkjet-printed thin-film transistors, *Adv. Sci.*, 2019, **6**, 1801445.
28 J. Kwon, Y. Takeda, K. Fukuda, K. Cho, S. Tokito and S. Jung, Three-dimensional, inkjet-printed organic transistors and integrated circuits with 100% yield, high uniformity, and long-term stability, *ACS Nano*, 2016, **10**, 10324–10330.
29 G. Mattana, A. Loi, M. Woytasik, M. Barbaro, V. Noël and B. Piro, Inkjet-Printing: A New Fabrication Technology for Organic Transistors, *Adv. Mater. Technol.*, 2017, **2**, 1700063.
30 W. Tang, Y. Huang, L. Han, R. Liu, Y. Su, X. Guo and F. Yan, Recent progress in printable organic field effect transistors, *J. Mater. Chem. C*, 2019, **7**, 790–808.
31 J. Zhang, B. Geng, S. Duan, C. Huang, Y. Xi, Q. Mu, H. Chen, X. Ren and W. Hu, High-resolution organic field-effect transistors manufactured by electrohydrodynamic inkjet printing of doped electrodes, *J. Mater. Chem. C*, 2020, **8**, 15219–15223.
32 S. Yang, S. Park, J. Bintinger, Y. Bonnassieux, J. Anthony and I. Kymissis, Employing Pneumatic Nozzle Printing for Controlling the Crystal Growth of Small Molecule Organic Semiconductor for Field-Effect Transistors, *Adv. Electron. Mater.*, 2018, **4**, 1700534.
33 Y. J. Kwon, Y. D. Park and W. H. Lee, Inkjet-printed organic transistors based on organic semiconductor/insulating polymer blends, *Materials*, 2016, **9**, 650.
34 X. Zhang, J. Jie, W. Deng, Q. Shang, J. Wang, H. Wang, X. Chen and X. Zhang, Alignment and Patterning of Ordered Small-Molecule Organic Semiconductor Micro-/Nanocrystals for Device Applications, *Adv. Mater.*, 2016, **28**, 2475–2503.
35 T. Schmaltz, G. Sforazzini, T. Reichert and H. Frauenrath, Self-assembled monolayers as patterning tool for organic electronic devices, *Adv. Mater.*, 2017, **29**, 1605286.
36 H. Wang, F. Fontein, J. Li, L. Huang, L. Jiang, H. Fuchs, W. Wang, Y. Wang and L. Chi, Lithographical Fabrication of Organic Single-Crystal Arrays by Area-Selective Growth and Solvent Vapor Annealing, *ACS Appl. Mater. Interfaces*, 2020, **12**, 48854–48860.
37 S. Park, G. Giri, L. Shaw, G. Pitner, J. Ha, J. H. Koo, X. Gu, J. Park, T. H. Lee, J. H. Nam, Y. Hong and Z. Bao, Large-area formation of self-aligned crystalline domains of organic semiconductors on transistor channels using CONNECT, *Proc. Natl. Acad. Sci. U. S. A.*, 2015, **112**, 5561–5566.
38 H. Minemawari, T. Yamada, H. Matsui, J. Tsutsumi, S. Haas, R. Chiba, R. Kumai and T. Hasegawa, Inkjet printing of single-crystal films, *Nature*, 2011, **475**, 364–367.
39 K. Kim, K. Nam, X. Li, D. Y. Lee and S. H. Kim, Programmed Design of Highly Crystalline Organic Semiconductor Patterns with Uniaxial Alignment via Blade Coating for High-Performance Organic Field-Effect Transistors, *ACS Appl. Mater. Interfaces*, 2019, **11**, 42403–42411.
40 Y. Li, D. Ji, J. Liu, Y. Yao, X. Fu, W. Zhu, C. Xu, H. Dong, J. Li and W. Hu, Quick Fabrication of Large-area Organic Semiconductor Single Crystal Arrays with a Rapid Annealing Self-Solution-Shearing Method, *Sci. Rep.*, 2015, **5**, 13195.
41 W. Zhao, J. Jie, Q. Wei, Z. Lu, R. Jia, W. Deng, X. J. Zhang and X. H. Zhang, A Facile Method for the Growth of Organic Semiconductor Single Crystal Arrays on Polymer Dielectric toward Flexible Field-Effect Transistors, *Adv. Funct. Mater.*, 2019, **29**, 1902494.
42 S. Duan, T. Wang, B. Geng, X. Gao, C. Li, J. Zhang, Y. Xi, X. Zhang, X. Ren and W. Hu, Solution-processed centimeter-scale highly aligned organic crystalline arrays for high-performance organic field-effect transistors, *Adv. Mater.*, 2020, **32**, 1908388.
43 W. J. Hyun, E. B. Secor, M. C. Hersam, C. D. Frisbie and L. F. Francis, High-resolution patterning of graphene by screen printing with a silicon stencil for highly flexible printed electronics, *Adv. Mater.*, 2015, **27**, 109–115.
44 Q. Ge, J. J. Kwok and Y. Diao, Flow-directed crystallization for printed electronics, *Acc. Chem. Res.*, 2016, **49**, 2756–2764.
45 L. Wang, C. Wang, X. Yu, L. Zheng, X. Zhang and W. Hu, Two-dimensional organic single-crystalline p-n junctions for ambipolar field transistors, *Sci. China Mater.*, 2020, **63**, 122–127.
46 C. Liu, T. Minari, X. Lu, A. Kumatani, K. Takimiya and K. Tsukagoshi, Solution-processable organic single crystals with bandlike transport in field-effect transistors, *Adv. Mater.*, 2011, **23**, 523.
47 T. Izawa, E. Miyazaki and K. Takimiya, Molecular Ordering of High-performance soluble molecular semiconductors and re-evaluation of their field-effecttransistor characteristics, *Adv. Mater.*, 2008, **20**, 3388–3392.

48 Z. Zhou, Z. Zhang, Q. Wu, X. Ji, J. Wang, X. Zeng, S. Feng and P. K. L. Chan, Inch-scale grain boundary free organic crystals developed by nucleation seed-controlled shearing method, *ACS Appl. Mater. Interfaces*, 2018, **10**, 35395–35403.

49 T. Sawada, T. Makita, A. Yamamura, M. Sasaki, Y. Yoshimura, T. Hayakawa, T. Okamoto, S. Watanabe, S. Kumagai and J. Takeya, Low-voltage complementary inverters using solution-processed, high-mobility organic single-crystal transistors fabricated by polymer-blend printing, *Appl. Phys. Lett.*, 2020, **117**, 033301.

50 S. Sung, W. Lee, M. M. Payne, J. E. Anthony, C.-H. Kim and M.-H. Yoon, Large-area printed low-voltage organic thin film transistors via minimal-solution bar-coating, *J. Mater. Chem. C*, 2020, **8**, 15112.

51 E. Stucchi, A. D. Scaccabarozzi, F. A. Viola and M. Caironi, Ultraflexible all-organic complementary transistors and inverters based on printed polymers, *J. Mater. Chem. C*, 2020, **8**, 15331–15338.

52 S. Lai, G. Casula, P. C. Ricci, P. Cosseddu and A. Bonfiglio, All-organic, low voltage, transparent and compliantorganic field-effect transistor fabricated by means of large-area, cost-effective techniques, *Appl. Sci.*, 2020, **10**, 6656.

53 V. Raghuwanshi, P. Saxena, S. Rahi, A. K. Mahato, I. Varun and S. P. Tiwari, Solution-processed flexible organic field-effect transistors with biodegradable gelatin as the dielectric layer: an approach toward biodegradable systems, *ACS Appl. Electron. Mater.*, 2020, **2**, 3373–3379.

54 T. Sawada, A. Yamamura, M. Sasaki, K. Takahira, T. Okamoto, S. Watanabe and J. Takeya, Correlation between the static and dynamic responses of organic single-crystal field-effect transistors, *Nat. Commun.*, 2020, **11**, 1–8.

55 Y. Jiang, Z. Liu, Z. Yin and Q. Zheng, Sandwich structured dielectrics for air-stable and flexible low-voltage organic transistors in ultrasensitive pressure sensing, *Mater. Chem. Front.*, 2020, **4**, 1459–1470.

56 G. Casula, S. Lai, L. Matino, F. Santoro, A. Bonfiglio and P. Cosseddu, Printed, low-voltage, all-organic transistors and complementary circuits on paper substrate, *Adv. Electron. Mater.*, 2020, **6**, 1901027.

57 H. Park, S. Yoo, J. C. Won and Y. H. Kim, Room-temperature, printed, low-voltage, flexible organic field-effect transistors using soluble polyimide gate dielectrics, *APL Mater.*, 2020, **8**, 011112.

58 Q. Mu, Z. Chen, S. Duan, X. Zhang, X. Ren and W. Hu, A low-temperature solution-process high-k dielectric for high-performance flexible organic field-effect transistors, *Front. Mater.*, 2020, **7**, 570002.

59 J. Choi, J. Kang, C. Lee, K. Jeong and S. G. Im, Heavily crosslinked, high-k ultrathin polymer dielectrics for flexible, low-power organic thin-film transistors (OTFTs), *Adv. Electron. Mater.*, 2020, **6**, 2000314.

60 V. Raghuwanshi, D. Bharti, A. K. Mahato, A. K. Shringi, I. Varun and S. P. Tiwari, High performance flexible organic field-effect transistors with barium strontium titanate gate dielectric deposited at room temperature, *ACS Appl. Electron. Mater.*, 2020, **2**, 529–536.

61 X. Ren, K. Pei, B. Peng, Z. Zhang, Z. Wang, X. Wang and P. K. Chan, A low-operating-power and flexible active-matrix organic-transistor temperature-sensor array, *Adv. Mater.*, 2016, **28**, 4832–4838.